Appl. Comput. Harmon. Anal. 28 (2010) 320–337

Contents lists available at ScienceDirect

Applied and Computational Harmonic Analysis

www.elsevier.com/locate/acha

2D Continuous Wavelet Transform of potential fields due to extended source distributions

M. Fedi [a,*], F. Cella [b], T. Quarta [c], A.V. Villani [c]

[a] Dipartimento di Scienze della Terra, Università Federico II di Napoli, Italy
[b] Dipartimento di Scienze della Terra, Università della Calabria, Italy
[c] Dipartimento di Scienza dei Materiali, Università di Lecce, Italy

ARTICLE INFO

Article history:
Received 31 March 2009
Revised 15 March 2010
Accepted 16 March 2010
Available online 18 March 2010
Communicated by Ginette Saracco

Keywords:
Continuous Wavelet Transform
2D
Potential field
Singularity detection
Depth from extreme points

ABSTRACT

We analyse the real Continuous Wavelet Transform 2D (CWT2D) of potential fields for the investigation of potential field singularities. We focus our attention to extended geological sources, in order to verify the reliability of this method with realistic fields. 3D space-scale representation (3D Scalogram) related to synthetic models were generated, showing the Wavelet Transform Modulus Maxima (WTMM) at each scale. The WTMM are related to the shape of the source, so defining some sort of source boundary analysis through the CWT. Wavelets of different order may help to gain resolution and define source features. Selecting a range of scales where the sources behave as if they are approximately isolated, the depth to the source may be estimated basing on the property that the lines joining the modulus maxima of the wavelet coefficients at different scales (WTMML) intersect each other at the edges of the causative body. Therefore, it is possible to manage the information contained in the wavelet transform of fields related to extended sources. In the real case of the anomaly gravity map of the Vesuvius area (Italy), we estimated the depth of the Mesozoic carbonate basement in the Pompei Basin. We showed also how the WTMML information can be integrated to that of another multiscale method, the Depth from Extreme Points (DEXP) transformation, which is also related to the source density distribution of a given region.

1. Introduction

The interpretation of potential field anomalies (gravity and magnetic) is not simple because it is inherently ambiguous. This ambiguity constitutes the main problem in the application of inversion techniques to obtain information about the sources.

The idea to draw source information from the upward continued potential field [23,10] can be well formalised in the frame of the Continuous Wavelet Transform (CWT). The CWT produces a scalogram, in which the WTMML converge to the singular points [18].

By this way the CWT allows localisation and characterisation of the singularities of a signal. According to several authors [20,21,15,28,11,30,31] the use of the derivatives of the Poisson kernel as wavelet implies that the CWT, as some scale a, is equivalent to the upward continuation of the q-order derivative of a potential field at the altitude $z_m = z + a$ (some scaling apart), where z_m is the altitude of the measurement surface.

* Corresponding author. Fax: +39 81 2538128.
E-mail addresses: fedi@unina.it (M. Fedi), fedcella@unical.it (F. Cella), tatiana.quarta@unisalento.it (T. Quarta), ada.villani@unisalento.it (A.V. Villani).

1063-5203/$ – see front matter
doi:10.1016/j.acha.2010.03.002

As concerns the CWT of the potential field due to isolated and simple sources, such as a line-mass or point sources, the WTMML converge below the scalogram to the source depth, preserving a straight line path on the whole range of scales. In real cases potential field anomalies are however the superposition of many effects, related to sources placed at different positions and with different dimensions. Such sources are often each one approximated by isolated bodies or by undulated interfaces. In this case, the WTMML of the shallower sources often dominate the ones due to the deeper sources, also at large dilations, making problematic the estimation of the local homogeneity and depth of the deeper sources. This problem has been analysed by Fedi et al. [11], which showed that low-pass filtering of the gravity anomalies could be needed to obtain good estimations about the deep sources.

Sailhac and Gilbert [29], Saracco et al. [30,31] used the Hilbert transform or the analytic signal of the q-order derivative of the Poisson kernel, defining complex 1D or 2D wavelets and analysed the modulus and the phase of the Hilbert transform. In particular Saracco et al. [31] interpreted magnetic field anomalies with 1D complex wavelet of order $q = 3$ and estimated the depth and the dip of the extended source by analysing the modulus and the phase. Sailhac and Gilbert [29] considered relationships between the multipolar expansion of the Newtonian potential caused by extended sources of simple geometrical shape (triaxial ellipsoid, cylinder and rectangular prism of constant density) and the WTMML of the modulus of the Hilbert transform, to the end of estimating the barycentre (using the monopole term) and the horizontal and vertical extent of the 3D sources (using the dipolar term). To such aim they analysed the properties of the WTMML at an intermediate-large range of scales, where the field tends to behave as that of an isolated singularity.

However, in many cases it is also interesting to obtain detailed information about the most specific parts of extended geological sources. For instance: interfaces, such as that relative to the carbonate-crystalline basements should be studied by analysing the WTMML properties at small scales where not the global, but the local characteristics of the source dominate. The relevance of this kind of study has not been enough taken into account in the current geophysical literature, but interesting applications were described in the case of a 1D wavelet analysis [11] and of the DEXP transformation [13]. So, we focus our paper toward this aspect, in order to define with some detail the features of 3D geological sources under a 2D wavelet analysis. To this end, in this paper we will use the q-order derivatives ($q = 1, 2, 3, 4$) of the 2D Poisson kernel as 2D wavelets, this meaning that we will utilise orders of derivation higher than in the above mentioned papers [29–31]. We first analyse synthetic cases of extended sources, trying to represent real-world geological sources, and then apply the method to the complex case of the vulcanite-carbonate basement at Mt. Vesuvius, the main volcano of the Quaternary Neapolitan volcanic area (Southern Italy).

2. Continuous Wavelet Transform 2D (CWT2D)

We define the CWT2D [3] of a signal $f \in L^2(R^2)$ as:

$$\mathbf{W}f(a, \mathbf{x}) = a^{-2} \int \psi^* \left(\frac{\mathbf{b} - \mathbf{x}}{a} \right) f(\mathbf{b})\, d\mathbf{b} \tag{1}$$

where $\mathbf{x}$ and $\mathbf{b}$ are vectors of real components (x, y) and (b_x, b_y), respectively; $\psi(\frac{\mathbf{b}-\mathbf{x}}{a})$ is an isotropic wavelet obtained by translation and dilation of the 'mother wavelet' $\psi \in L^2(R^2)$; $a \in R^+$ is the scale parameter and the symbol '$*$' indicates complex conjugation. In Eq. (1) we used a normalisation preserving the L^1 norm, which enhances the information contained at small scales. Antoine et al. [3], have also defined a 2D anisotropic wavelet $\psi(\frac{r_{-\theta}(\mathbf{b}-\mathbf{x})}{a})$ where $r_{-\theta}$ is the rotation operator acting in the usual way. The anisotropic wavelets are used to detect oriented features in an image, for instance, in the classical problem of edge detection or in directional filtering. Here we however analyse potential fields using the q-order horizontal derivatives of the Poisson kernel as wavelets (see later in the Chapter 3), which correspond in the 2D case to isotropic wavelets, according to [11,13,15,20,28–31]. This because only Poisson wavelets enjoy the main property of allowing the Continuous Wavelet Transform matching the upward continued derived field, some constant apart, which is indeed a feature giving physical consistency to the transformed field (Sections 3 and 4).

The wavelet has to satisfy the admissibility condition:

$$\int \psi(\mathbf{x})\, d\mathbf{x} = 0 \tag{2}$$

Besides, the wavelet ψ can have a few vanishing moments:

$$\int x^l y^m \psi(\mathbf{x})\, d\mathbf{x} = 0, \quad 1 \leqslant l + m \leqslant q \tag{3}$$

this last condition determining the ability of the Wavelet Transform to detect singularities in the (q)th-order derivative of the signal [18].

The scalogram produced by the CWT2D is a 3D volume. Each plane of the Scalogram contains the values of $\mathbf{W}f(a, \mathbf{b})$ relative to the scale a. Assuming a smoothing function $\phi(x, y)$ and wavelets [1]:

$$\psi_x(x, y) = \frac{\partial \phi(x, y)}{\partial x} \quad \text{and} \quad \psi_y(x, y) = \frac{\partial \phi(x, y)}{\partial y} \tag{4}$$

the CWT assumes a vectorial form (Appendix A, Eq. (A.7)) for any function $f(x, y) \in L^2(R^2)$:

$$\mathbf{W}f(a, \mathbf{x}) = a\nabla\{\phi_a * f\} \tag{5}$$

$$\text{where } \phi_a = \frac{\phi(x/a, y/a)}{a^2} \tag{6}$$

The WTMM are the maxima of $Mf(a, \mathbf{x})$ in the direction $Af(a, \mathbf{x})$, at each scale, where:

$$Mf(a, \mathbf{x}) = \left|\mathbf{W}f(a, \mathbf{x})\right| = \left[\left(W_x f(a, \mathbf{x})\right)^2 + \left(W_y f(a, \mathbf{x})\right)^2\right]^{1/2} \tag{7}$$

and

$$Af(a, \mathbf{x}) = \mathrm{tg}^{-1}\left[\left(W_y f(a, \mathbf{x})\right)/\left(W_x f(a, \mathbf{x})\right)\right] \tag{8}$$

Mallat and Zhong [17] and Mallat and Hwang [16] showed that the modulus maxima contain much of the information owned to a given dataset. They actually re-phrased the technique of Canny [6] in terms of the CWT2D and called Multiscale Edge Detection 2D (MED2D) the search of maxima at each scale. See Appendix A for more details.

3. The CWT2D in potential field theory

As previously stated, each plane of the 3D scalogram contains the values $Wf(a, \mathbf{x})$ at the scale a.

It can be shown [20,15] that, using as wavelet the q-order derivatives of the Poisson kernel (Green's function for potential fields), the CWT of potential field data is equivalent at each scale a to the q-order horizontal derivative of the field upward continued at the altitude a, some scaling apart. For an isolated point source, WTMML are straight lines converging to the point source location. When sources are not isolated reciprocal interference may cause distortion of the straight path of the WTMML, especially at an intermediate range of scales, making problematic the depth estimation of the sources. The interference effects for 2D extended structures of polygonal cross-section was discussed in Fedi et al. [11]. So, the WTMML distribution can assume very complex paths in the 3D scalogram, in case of extended 3D sources: the convergence of the WTMML to the singularity locations (edges of the causative body) may occur only selecting an appropriate range of scales, for which each singularity can be considered approximately isolated. For an isolated singularity (the anomaly field depends by the coordinates of only one point) the Hölder regularity degree β is a constant at every point of the harmonic region and the WTMML are straight lines.

The harmonic region ([4], page 47) is constituted by the points, external to the source distribution, where the potential $U(x, y, z)$ satisfies the Laplace equation $\nabla^2 U(x, y, z) = 0$.

In the case of multiple sources or extended bodies of finite size, because of the interference, β varies with the distance between the observation point and the source [27,29] and WTMML are curved lines. In this case, it is necessary to select a range of scales where the WTMML is straight to estimate depth and regularity degree. We will show that the best resolved singularities are the vertices of the most isolated parts of the causative body.

Consider now the q-order derivatives of the Poisson kernel 2D:

$$p(\mathbf{x}) = \frac{1}{2\pi}\left(1 + |\mathbf{x}|^2\right)^{-3/2} \tag{9}$$

whose dilated form is [29]:

$$p_a(\mathbf{x}) = \frac{1}{2\pi}a\left(a^2 + |\mathbf{x}|^2\right)^{-3/2} \tag{10}$$

According to Eq. (5) we can write for the gravity field:

$$\mathbf{W}g_m(p, \mathbf{x}, a) = a\nabla\{p_a * g_m\} = a\nabla g_z(\mathbf{x}, a) \tag{11}$$

where $a = z - z_m$, $g_m(\mathbf{x})$ are the experimental data known at the level z_m, and $g_z(\mathbf{x})$ are the gravity field values upward continued from the level z_m to the level z. We can generalise Eq. (10) for any order q:

$$\mathbf{W}g_m^{(q)}(p, \mathbf{x}, a) = a^q\nabla^{(q)} g_z(\mathbf{x}, a) \tag{12}$$

with components:

$$\mathbf{W}g_m^{(q)}(p, \mathbf{x}, a) = \begin{pmatrix} W_x g_m^{(q)} = \psi_a^{x,q} * g_m = a^q \frac{\partial^q g_z(\mathbf{x}, a)}{\partial x^q} \\ W_y g_m^{(q)} = \psi_a^{y,q} * g_m = a^q \frac{\partial^q g_z(\mathbf{x}, a)}{\partial y^q} \end{pmatrix} \tag{13}$$

where

$$\psi^{x,q}(x, y) = \frac{\partial^q p(x, y)}{\partial x^q} \quad \text{and} \quad \psi^{y,q}(x, y)(x, y) = \frac{\partial^q p(x, y)}{\partial y^q}$$

The choice of the q-order derivative of $p(\mathbf{x})$, or equivalently the number q of vanishing moments of the wavelet, depends on the Hölder regularity degree β [18] of g_z. Only if $q > \beta$, WTMML exist which intersect each other below the scalogram,

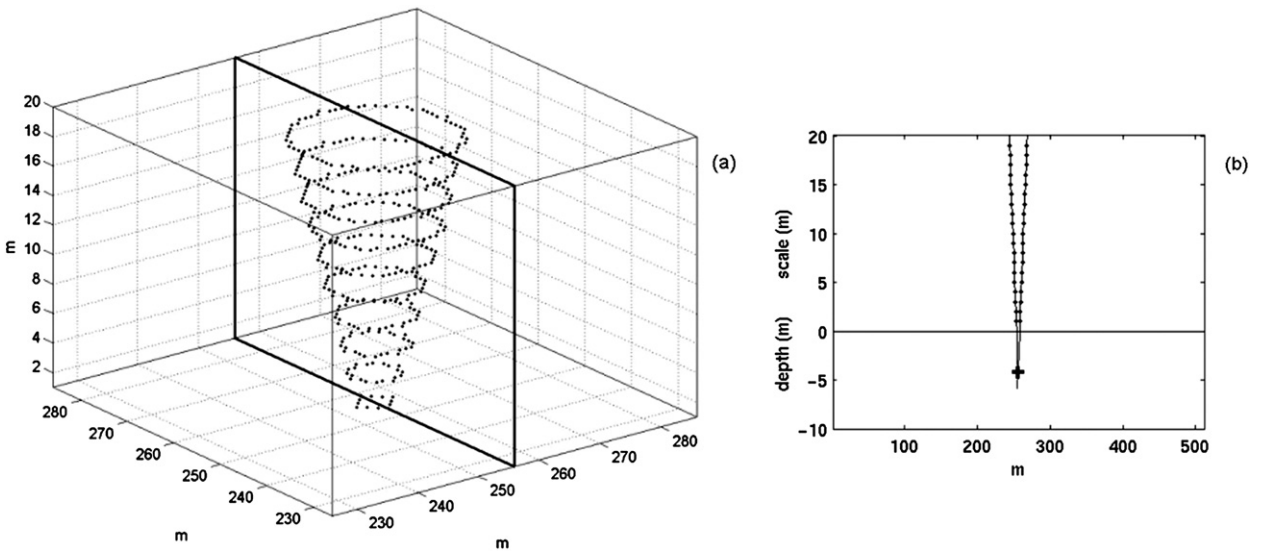

Fig. 1. (a) WTMM of the gravity anomaly gradient modulus due to a pole-source located at $(512, 512, -4)$ m; (b) WTMML of one vertical section containing the source.

in correspondence of the edges of the source. It is clear that for q-order wavelets, the CWT2D will depend on the q-order partial derivatives of g_z and WTMM will correspond to the modulus maxima of the q-order gradient of g_z at different levels. For $q > 1$ (see Appendix B) the analysing wavelets can be selected in various ways.

The most direct method to estimate the source position is the so-called geometrical method, which defines the source depth at the intersection of the field WTMML extrapolated into the source region [20]. A simple, but instructive, example is that of an isolated pole source, such as that shown in Fig. 1, located at $(512, 512, -4)$ m. Using wavelets of order $q = 1$ the WTMM of the gradient modulus describe a cone, whose apex coincides with the source location. In Fig. 1b WTMML are shown relative to a vertical section (solid black line in Fig. 1a) extracted by the 3D scalogram. The best fit lines of the two WTMML intersect one each other at the right source depth. This geometric characteristic is independent on the degree of homogeneity of the source [14]. In the case of multiple sources the interference between their gravity effects will curve the WTMML and the source may be locally considered as isolated only using an appropriate order of derivative and within a limited range of scales, where the WTMML are approximated by straight lines. For extended sources the various degree derivatives of the field allow different source characteristics to be evidenced. For instance, at large scales and at a low derivative order, WTMML intersecting at mass centre of the source occur. For high derivative orders, see Section 5 (e.g., Figs. 3f, 5f, 8c, 8d), WTMML intersecting near the edges of the body are likely to be observed. This deterministic approach may cause some imprecision on the source parameter estimates, when complicated real cases are involved. It is however commonly used in geophysical literature and it has been validated by practical experience [11,13,15,28,30,31].

Statistical methods allow good estimates of the average values of some sources characteristics such as depth, geometry, magnetisation or density contrast. Pilkington and Todoeschuck [24] and Maus and Dimri [19], under the assumption of a 3D fractal source distribution, derived general relationships between the scaling properties of the field power spectrum and the source power spectrum which allow to estimate the characteristics of the source.

4. The DEXP Transformation

Several authors [11,15,18,20,21,28–31] have interpreted the anomaly fields using a deterministic approach. By using the derivatives of the Poisson kernel as wavelets, they have estimated source depth and structural index by applying both the geometrical method and the best depth method based on dilation property of Poisson Kernel and covariance and dilation properties of the wavelet transform. We used here a different approach [13,34] to study homogeneous fields $f_z(\mathbf{x}, a)$. We studied the behaviour of the scale function τ_q:

$$\tau_q(a, \zeta) = -N_q \frac{a - \zeta}{a - z_0} \tag{14}$$

where q is some order of partial derivative of the potential field, a is the scale, the variable ζ is our "depth guess" for the unknown depth to the source z_0 and the structural index N_q [25,34] is related to the homogeneous degree of the gravity field n_g and to q by: $N_q = -n_g + q$.

The scale function is a dimensionless quantity which characterises the scaling behaviour of a given field and enjoys interesting properties. For instance, when $a \gg -z_0$, $\tau_q(z, 0) \to -N_q$.

Another main property is that when ζ is equal to z_0, the scale function is constant function of the scale a and its value is equal to $-N_q$.

Based on this scale function theory, he also defined a new transformation for potential fields, called Depth from Extreme Points (DEXP) transformation. He proved that for simple sources whose singular point is at (x_0, y_0, z_0) the DEXP transformed field of order q:

$$\Omega f^{(q)} = a^{(\frac{q}{2}+\alpha)} \frac{\partial^q f_z(\mathbf{x}, a)}{\partial z^q} \tag{15}$$

has an extreme point in the harmonic region at $x = x_0$, $y = y_0$, $z = -z_0$, where α, called scaling exponent in Fedi [13], is the half of N_0. It is interesting to understand this relevant property of homogeneous potential fields by comparing the DEXP transformation (Eq. (15)) to the CWT of the same order q:

$$W_x f^{(q)} = a^q \frac{\partial^q f_z(\mathbf{x}, a)}{\partial x^q}, \qquad W_y f^{(q)} = a^q \frac{\partial^q f_z(\mathbf{x}, a)}{\partial y^q} \tag{16}$$

It is evident that $\Omega f^{(q)}$ has a similar form to that of $W f_x^{(q)}$ (or $W f_y^{(q)}$) excepted the variable of derivation and the exponent of the power law factor, which in the DEXP formulation is $q/2 + \alpha$ and so depends on both the order (q) and the source properties (through the structural index N_0), while in the CWT formulation depends only on the order q.

Analysis of the fields along WTMML allows estimations of the structural index and the source depth no matter CWT or DEXP is considered. When N_q can be estimated or expected to do not vary much in some region, DEXP transformation will provide a very meaningful 3D description of the main source distribution [13]. We will apply the DEXP transformation with $q = 2$ to the Campanian Plain gravity data (Section 6).

5. WTMML for potential field anomalies due to extended geological sources

A simple inspection of Eq. (1) shows immediately that the CWT is really redundant: $f(x, y)$ is in fact unfolded from two variables (x, y) to three variables (x, y, a). But, it is well known that the main information is mostly contained in a small subset of the coefficients, namely those corresponding to the WTMML. The ensembles of the WTMML may help to locate edges of geological bodies. In this section we will analyse, in the 3D scalogram, WTMM produced by applying the Multiscale Edge Detection 2D (MED2D) to the gravity fields generated from extended geological sources. In fact, up to now, the MED2D method has concerned isolated simple sources, such as poles, line-mass or right prismatic bodies of constant density [29]. In this paper we consider instead gravity anomaly maps produced by more complex sources, which may better characterise geological sources in the real-world. Examples of these sources are the prismatic body of constant density with a tilted side (Case A and Case B) and the double fault (Case C). Gravity anomaly maps sized (256×256) km^2 and with 1 km sampling interval were computed applying the Talwani formula [32] to 60 rectangular prisms of 0.1 km thickness, used to approximate the 3D source shape.

5.1. Case A: gravity anomaly produced by a prismatic body having an up-going tilted side

The first source we consider is a prismatic body of constant density with an up-going tilted side. It may be used to approximate the shape of a geometrical element often occurring within geological structures, that is the normal/inverse fault. It results from the displacement between two rock volumes along a tilted plane causing an oblique density contrast. In this case, the upper volume (namely, the "hanging wall" in geological terms) is denser. The gravity anomaly produced by such source is shown in Fig. 2. 3D WTMM are shown, with scales a ranging from 1 to 28 km, with a 3 km step (Fig. 3a). WTMM are also shown for increasing derivative order q (Figs. 3c and 3e). As said previously, the geometrical method requires that at least two WTMML are intersecting at the edges of the body.

Our problem is hence to select:

a) an appropriate order q for Poissonian wavelets $\psi^{x,q}$ and $\psi^{y,q}$ in order to detect at least two WTMML converging below the scalogram; if these two WTMML lie entirely on a single plane, we can select this plane for a simpler inspection.
b) a range of scales where the two WTMML are well approximated by two straight lines.

By these conditions WTMML can be fitted by straight lines that intersect each other at the edges of the body, below the scalogram. The WTMML relative to the vertical section marked by solid black line in Figs. 3a, 3c and 3e, are shown in Figs. 3b, 3d and 3f respectively.

WTMM for $q = 1$ are shown in Fig. 3a. They correspond to the modulus maxima of ∇g_z. At the finest scales WTMM observed at the planes corresponding to different altitudes a are much related to the horizontal section of the upper part of the body.

The vertical section shown in Fig. 3b, parallel to the x–z plane, allows the estimation of the source extent along the x-axis. Obviously a vertical section parallel to the y–z plane will allow the estimation of the y-axis source extent. Only one WTMML occurs in correspondence of the vertices (A) and (B) of the source, so that the geometrical method cannot be applied for depth estimation. Besides, we observe that the WTMML shows a more curved path in correspondence of the vertex B, because of the tilted side of the body.

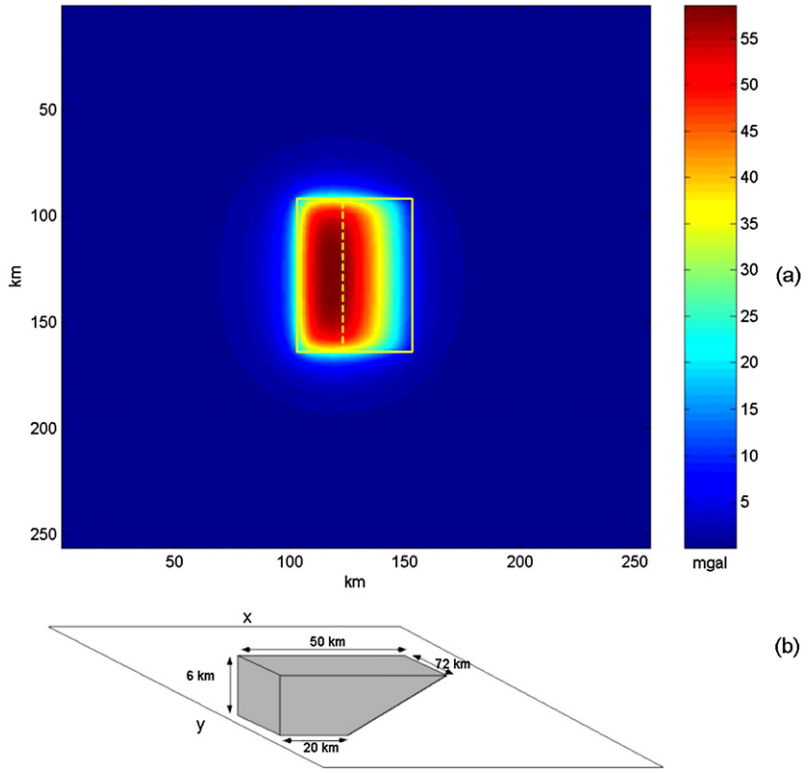

Fig. 2. (a) Gravity anomaly map produced by the source model shown in (b) placed at a 1 km depth to the top.

We therefore turn to WTMM for $q = 2$ (Fig. 3c). They correspond to the modulus maxima of $\nabla(\frac{\partial g_z}{\partial x})$ (Eq. (B.10)). We observe the WTMML relative to the vertical section in Fig. 3d. In this case it is possible to estimate only the depth to the vertex A of the model.

Consider finally WTMM for $q = 3$ (Figs. 3e and 3f). They correspond to the modulus maxima of $\nabla(\frac{\partial^2 g_z}{\partial x^2})$ and we observe a very complex path. The WTMML relative to a vertical section are shown in Fig. 3f. In this case we can well estimate the depth of the most shallow vertices (A and B). Note that a WTMML closely departs from vertex C, while the coincidence of the x-axis positions of vertices D and A cannot provide a good resolution to solve for the vertex D.

Besides, let us observe that, due to the closeness of the vertices B and C, WTMML lose their straight path at the highest scales (Figs. 8d and 8f), this meaning that the number of scales useful to the estimation process can be correspondingly reduced.

We have analysed the WTMML lying on a vertical plane passing through the barycentre of the source and parallel to the x–z plane in order to detect the vertices of the vertical section of the body parallel to the x-axis. We have shown that for increasing order q-derivative it is possible to detect more and more details on the shape of the body and obviously the WTMML relative to the vertices of the shallow part of the body section furnish a greater contribution to the gravity anomaly and hence the may by more easier detected. The WTMML relative to the deeper vertices are severely influenced by those relative to the upper part of the source and an order $q > 3$ must be used in order to detect them.

A wavelet of order q have q of vanishing moments (Eq. (3)) and it is able to remove polynomial trends of degree $< q$, present in the anomaly field due to the interferences of each vertex with all the others. Such interference effects were already studied for 2D structures [11, appendix C], where the case of an undulated interface was considered, actually separating two source distributions of constant density. The resolution power of the method was shown to depend on the relative horizontal distance among the vertices and on their depths. We considered also the case of two line-masses and we showed the improvement obtained in depth estimation using wavelets of increasing order q.

In order to try to detect the vertices of the vertical section of the body parallel to the y-axis, we consider the WTMML lying on a vertical plane passing through the barycentre of the source and parallel to the y–z plane. In this case for $q = 2$ and $q = 3$ it is necessary to analyse the modulus maxima of $\nabla(\frac{\partial g_z}{\partial y})$ and $\nabla(\frac{\partial^2 g_z}{\partial y^2})$ respectively.

5.2. Case B: gravity anomaly produced by a prismatic body having a down-going tilted side

Consider now a prismatic body of constant density contrast having a down-going tilted side. Also this source may be assimilated to the geometry of a rock volume faulted along a tilted sliding surface, with the occurrence of a lateral density

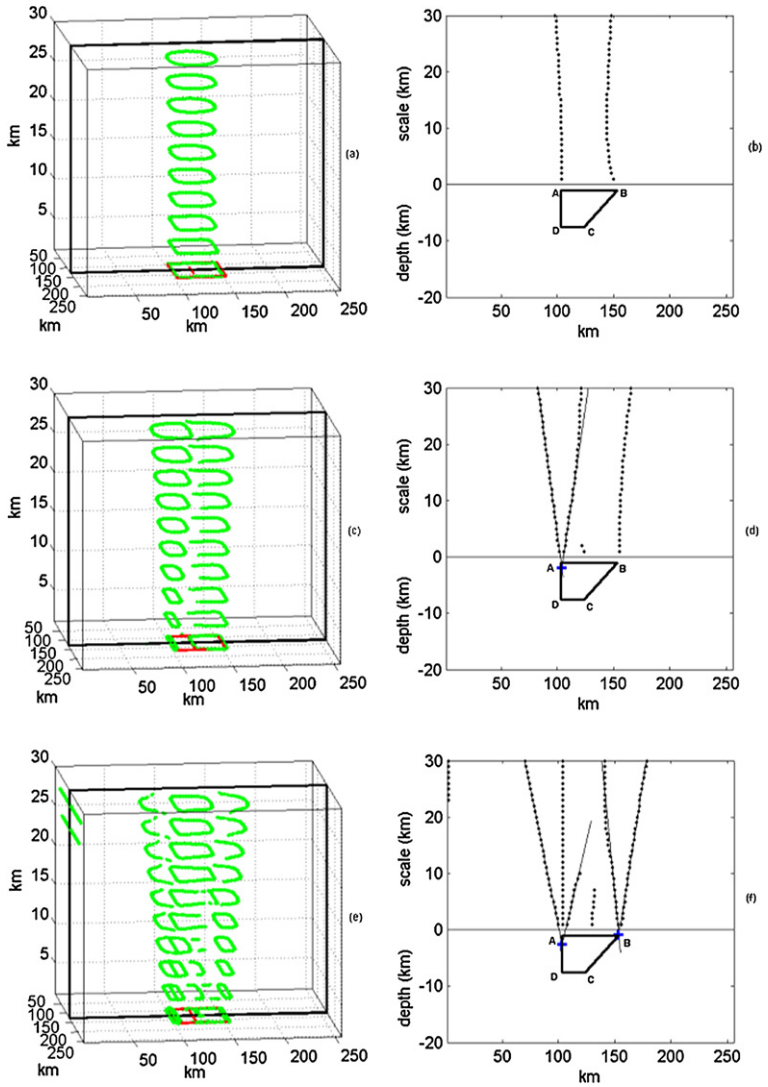

Fig. 3. (a), (c) and (e) 3D scalogram showing WTMM calculated using a wavelet of order $q = 1, 2$, and 3, respectively; (b), (d) and (f) WTMML in the vertical sections (solid black line) extracted by the 3D scalogram (a), (c) and (e), with overlapped the best-fit lines converging at the most superficial edges of the body below the scalogram.

contrast. Unlike the previous case, the lower volume (namely, the "footwall" in geological terms) is denser. The gravity anomaly produced by such source is shown in Fig. 4.

We again use wavelets of increasing order q (Fig. 5) as in Fig. 3. WTMML lying on vertical sections, marked by solid black lines in Figs. 5a, 5c and 5e, are respectively shown in Figs. 5b, 5d and 5f.

There are significant differences among Figs. 3 and 5 with respect to the previous case:

- using wavelets of order $q = 1$ (Fig. 5b), we observe that the WTMML relative to the vertex B, is bent in an opposite way to that of Fig. 3b because of the different slope of the side BC. We deduce, therefore, from the WTMML path, the slope of the fault; this information is very important from a geologic point of view;
- using wavelets of order $q = 3$ (Fig. 5f), it is now possible to estimate the depth of the vertex C, even if with a greater uncertainty, besides that of A and B vertices.

In conclusion, the WTMML analysis using wavelets of increasing order, allows again a fine recovering of the most shallow part of the body (vertices A and B), and it is possible to estimate also the deepest vertex positions, depending on the degree of interference due to the geometric position of all the vertices of the body.

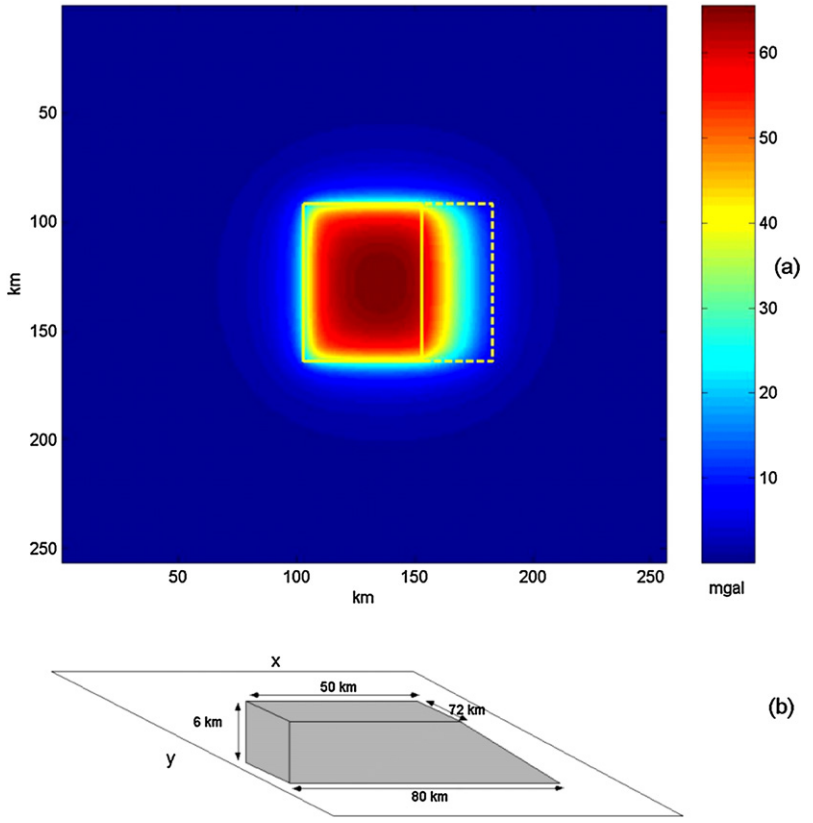

Fig. 4. (a) Gravity anomaly map produced by the source model in (b) placed at a 1 km depth to the top.

5.3. *Case C: gravity anomaly due to a double fault model*

A double fault model is here used to reproduce, in a simplified way, the gravity anomaly (Fig. 6a) due to a case typical of shallow crustal structure subject to a compressive stress (Fig. 6b). It simulates multiple thrusts in which size and geometry of the inverse faults are coherent with the real case that is found along the central Apennines [22], Italy, namely a typical thrust/fold belt. In particular the structure labelled M (Fig. 6b) has the top placed at 1 km depth, while that labelled N (Fig. 6b) has the top at 1.5 km depth.

The WTMM relative to wavelets of order $q = 1, 2, 3$ and 4 are again represented in a 3D volume (Fig. 7). They correspond to the modulus maxima of $\nabla(\frac{\partial^q g_z}{\partial x^q})$, for $q = 1, 2, 3, 4$ respectively. We observe that the paths of the WTMM are as more complex as the order of the wavelet increases. The WTMML lying on vertical sections, marked by solid black line in Figs. 7a, 7b, 7c and 7d, are shown in Figs. 8a, 8b, 8c and 8d respectively.

Using wavelets of order $q = 1$ (Fig. 8a), the WTMML do not well locate the shallow vertices of the structures. For $q = 2$ (Fig. 8b), the shallow vertices A, B, E and F are well detected and for $q = 3$ (Fig. 8c), the geometrical method yields even better depths estimation. In Fig. 8c however the effects related to the deeper vertices C, H and G distorts the paths of the WTMML relative to the shallow vertices A, B, E and F, at scales greater than 10 km.

Using wavelets of order $q = 4$ (Fig. 8d) it is possible to locate also the deepest vertex D. The x-axis proximity of the deeper vertices C, H and G to the most shallow A, B and E respectively, does not allow a clear detection of them, since the WTMML of the most shallow vertices dominate.

By the examples in Figs. 3, 5, 7 and 8 we tried to show the ability of the 2D CWT to isolate the effects from the different local zones defining a complex 3D body, where "singular points" may represent a good model for deriving local source properties. Nevertheless, our CWT analysis may be even more complete, if we add the structural index estimation to the above described depth estimation by a geometrical method. For the sake of simplicity we do not show this estimation for the several WTMML shown in Figs. 3 (b, d, f), 5 (b, d, f) and 8, referring to other papers, such as [13,28–30]. As an example, we show (Fig. 9) the estimation of the structural index and of the depth to the source made for the upper vertex B in Fig. 8d, by using the scale function of order $q = 4$. When ζ is equal to 1.5 km, τ_4 becomes approximately flat and, according to the properties of the scale function (Section 4), we can estimate a depth to the source z_0 equal to 1.5 km and a structural index equal to 3.2, corresponding with a good approximation to a singular point characteristic of a contact ($N_0 = -0.8$, for a gravity field). Note that the depth estimated by the scale function well corresponds to the depth estimated by the geometrical method (Fig. 8d, vertex B).

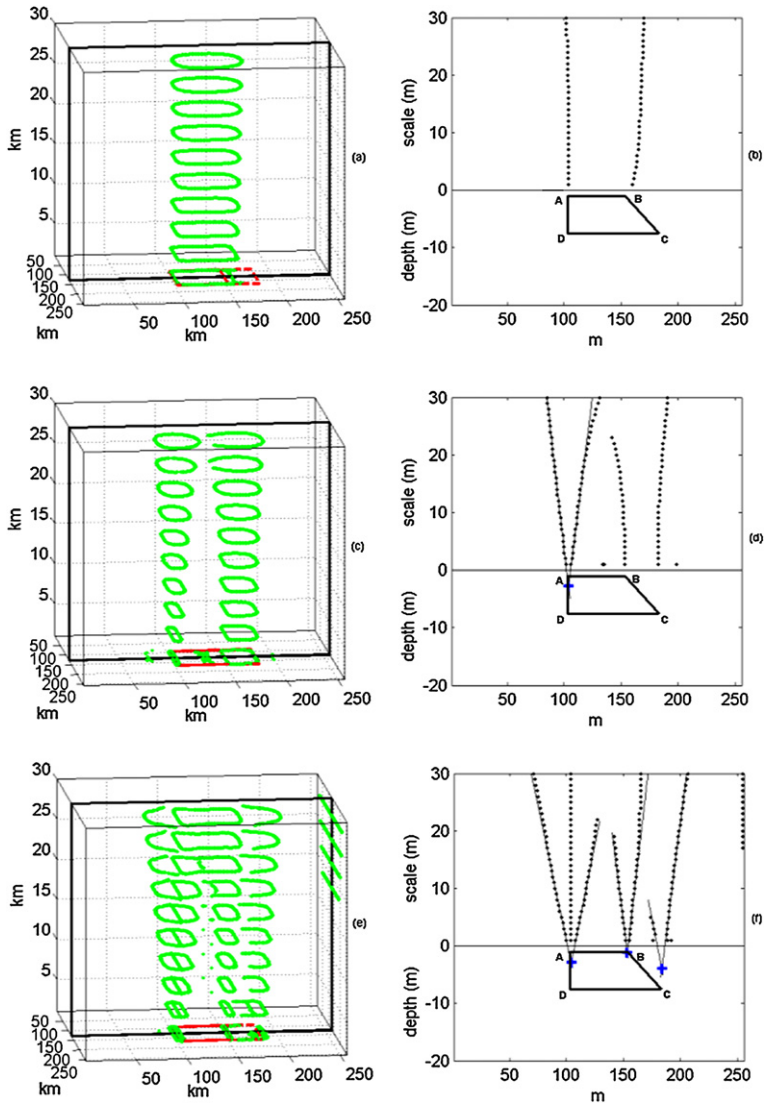

Fig. 5. (a), (c) and (e) 3D scalogram showing WTMM calculated using a wavelet of order $q = 1, 2$, and 3, respectively; (b), (d) and (f) WTMML in the vertical sections (solid black line) extracted by the 3D scalogram (a), (c) and (e), with overlapped the best-fit lines converging at some edges of the body.

5.4. CWT allows estimation of source boundaries

WTMML are defined in this paper in a 3D half-space. Starting by the WTMM at the finest scale (for example on the plane of equation $a = 1$) each WTMML is obtained searching along the scale axis the nearest WTMM on the subsequent plane (of equation $a = 2$) and so on. The WTMML is obtained as the line joining across scales these selected points. By using the Poisson wavelets of Eq. (13), the wavelet modulus maxima defined at each scale a can be related to the boundaries of geological sources. In fact, Eqs. (15) show that the wavelet transform of order q at some scale a is nothing but the horizontal derivative of order q of the measured potential field continued at that scale, some normalisation apart. So, at each scale a, the modulus maxima can be used to describe the source boundaries, according to the so-called boundary analysis, described in many papers, such as [2,12]. This is indeed evident in Figs. 3; 5; 7 (left side). Due to the dilation and to the theory described in this paper, however, small dilations should be the most suitable in terms of boundary analysis. We may hence observe that:

a) the best detection of the source boundaries is obtained from the modulus maxima of the wavelet transform as closest we are to the sources, that is at the observation scale;
b) the source boundary definition may be also more refined by extrapolating the WTMML in the source region, and studying their reciprocal intersection: this is shown in the same figures on the right side, where meaningful sections of the WTMML relative to the sources are shown.

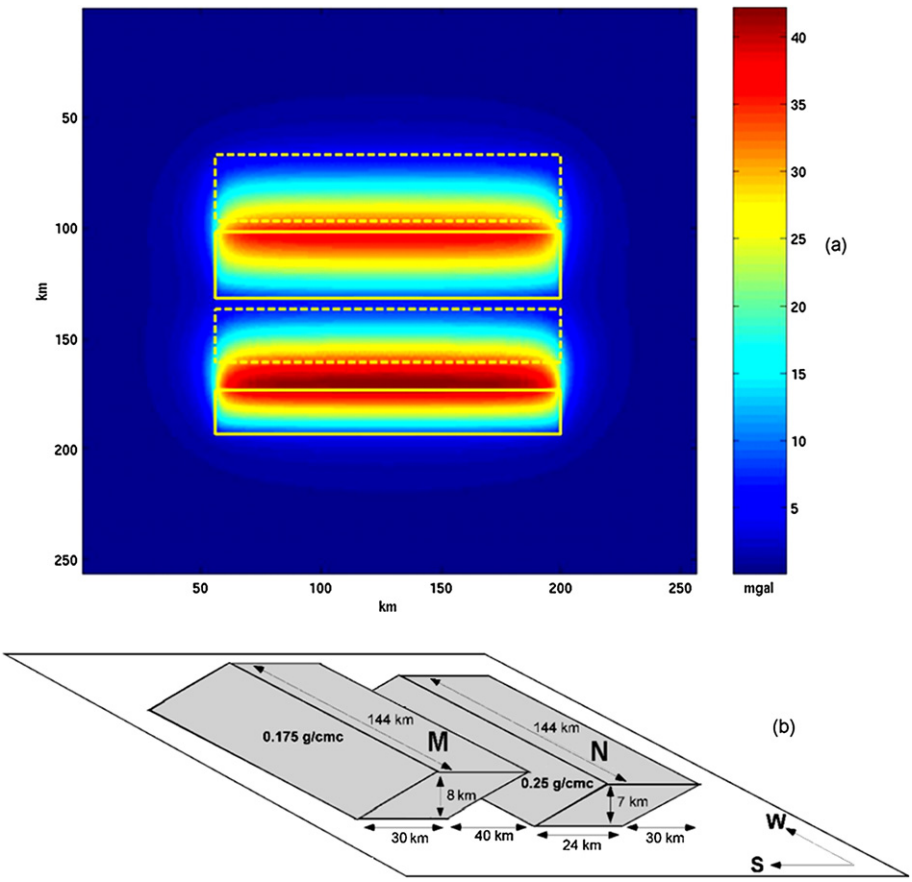

Fig. 6. (a) Gravity anomaly map produced by the source model in (b) made by two sources (M) and (N) placed at $h_M = 1$ km depth to the top, $h_N = 1.5$ km depth to the top, respectively.

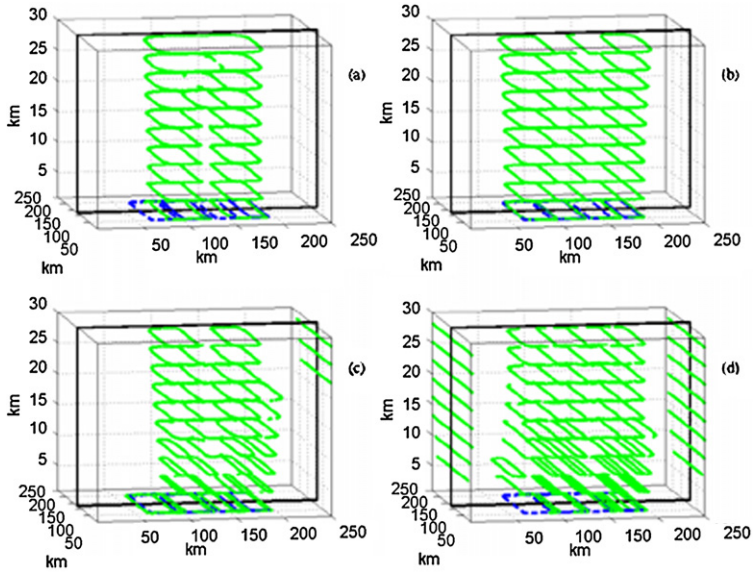

Fig. 7. (a), (b), (c) and (d): 3D scalogram showing WTMM calculated using a wavelet of order $q = 1, 2, 3$ and 4, respectively.

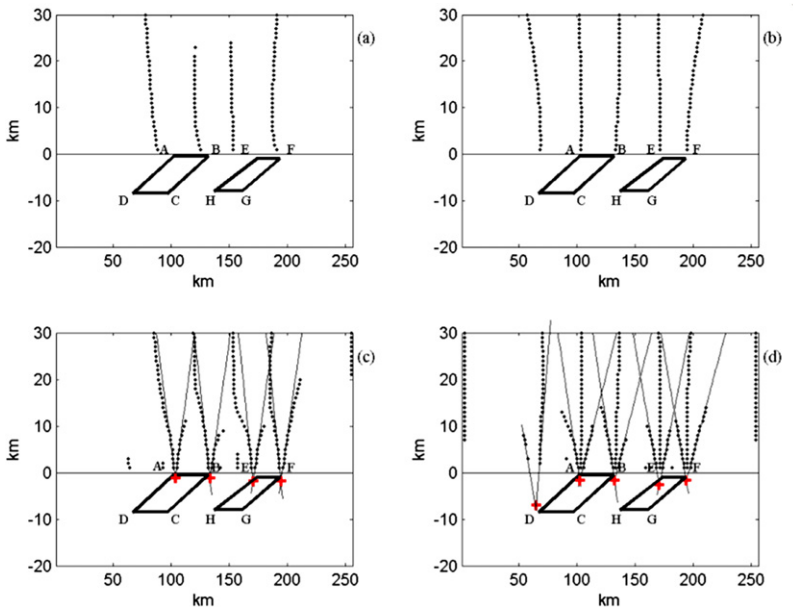

Fig. 8. WTMML in the vertical sections extracted by the 3D scalogram (solid black lines in Fig. 7), with overlapped the best-fit lines converging at some edges of the body below the scalogram.

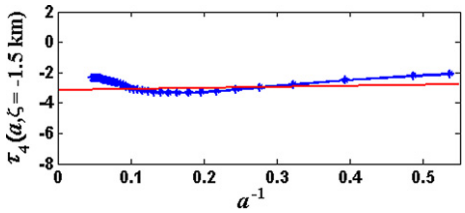

Fig. 9. Scale function of order $q = 4$ for the central WTMML converging to vertex B in Fig. 8d. It was computed for a guess depth $\zeta = 1.5$ km, fairly well indicating a homogeneous degree $n_q = -3$, this implying $N_q = -1$.

6. Real case: applications to the Vesuvius gravity data (Italy)

The technique previously described has been applied to the Bouguer anomaly map of the area including the Somma-Vesuvius complex. It rises within the south-eastern side of the Campanian Plain (Southern Italy) that is bounded to the N, E and S by the Apennine chain and, to the W, by the Tyrrhenian Sea (Fig. 10). It was formed when tensional stresses and crustal thinning due to the opening of the Tyrrhenian Basin caused during Plio-Pleistocene a tectonic depression that was filled by a thick cover of marine and volcanic sediments laying on the mesozoic carbonate basement. Since 0.4 Myr B.P. the extensional phase was accompanied by an intense volcanic activity fed by potassic magmatism, ranging from lentitic tephrite to lentitic phonolite where actually the Somma-Vesuvius rises. After a long quiescence began 0.3 Myr B.P., it re-started after 37 000 yr B.P. continuing with different kinds of volcanism (both quiet lava emissions and strong explosive eruptions) [9,26].

The gravity anomaly in Fig. 11 is the so-called *Bouguer gravity anomaly*. Such anomaly is defined at $P(x, y, h)$, where h is the distance above the geoid (the equipotential surface of the Earth approximately at mean sea level) as ([4], page 144):

$$\delta g_{cb} = g_{obs} - g_0 - g_{fa} - g_{sb} - g_t$$

where:

g_{obs} is the measured gravity value corrected for tidal and instrumental drift variations;

g_0 is the theoretical gravity or normal gravity on the reference ellipsoid, which is the equipotential surface of a uniform Earth. Differences in height between these two surfaces rarely exceed 100 m and generally fall below 50 m;

g_{fa} is the free-air correction, to take into account the gravity variation of g_0 with h;

g_{sb} is the Bouguer correction to take into account the presence of mass between the sea level and the height h of the observation point. This correction approximates these masses with a homogeneous infinitely extended slab of thickness h;

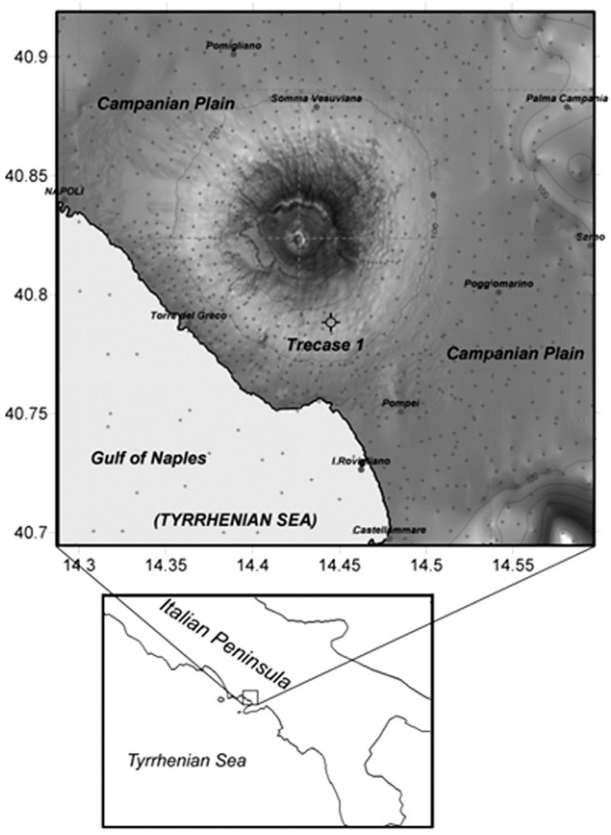

Fig. 10. Sketch map of the Somma-Vesuvius area. The Somma-Vesuvius complex is located within the Campanian Plain. The plain is filled by marine and volcanic sediments of Plio-Pleistocenic age and formed by subsidence of the Mesozoic carbonate basement, due to the crustal thinning toward the Tyrrhenian Basin and to the Apennine chain building.

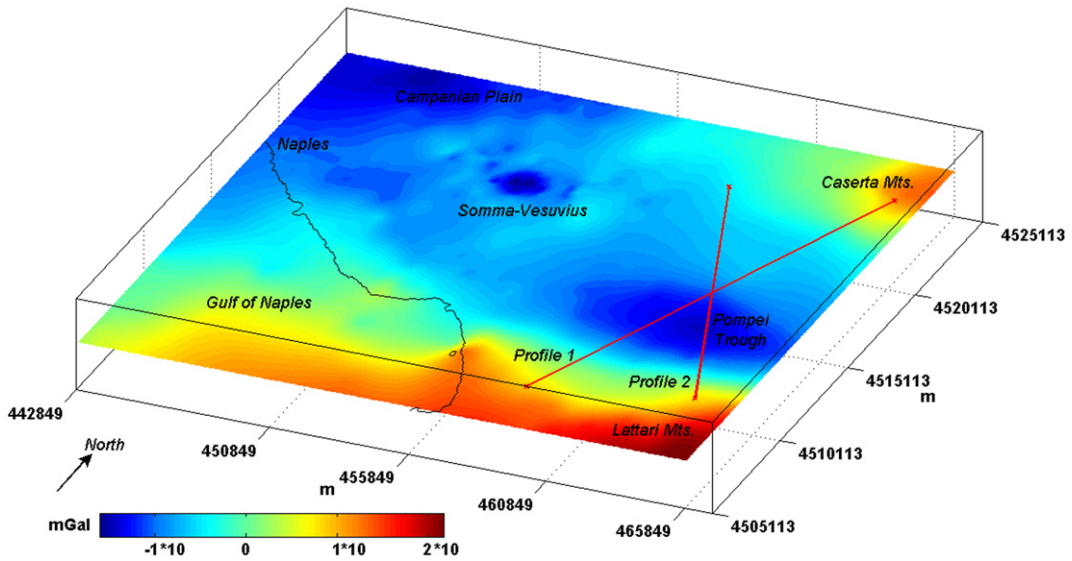

Fig. 11. Bouguer gravity anomaly map in the investigated area. Also shown Profiles 1 and 2 (red segments) analysed by the DEXP method in Figs. 14 and 15. UTM coordinates in metric units (Zone 33N). (For interpretation of the references to color in this figure legend, the reader is referred to the web version of this article.)

g_t is the terrain correction to take into account the shape of the topography. It is an essential step in places of moderate to extreme topographic relief.

The Bouguer anomaly field of the studied area (Fig. 11) is characterised by a broad low extended toward the north-westward side of the studied area. A second, less intense, negative anomaly is located between Poggiomarino and Pompei, and a third one is centred just in correspondence of the Somma-Vesuvius complex, presumably related to its shallow volcanic structure. Two highs are present in correspondence of the carbonate outcrops at the southern and eastern ends of the investigated area.

Serious questions concern the structural setting of the Somma-Vesuvius district, with clear reference to the high volcanic hazard due to the dense population living in this area. One of them is the shallow structure of the Mesozoic carbonate basement buried by the volcanic relief and by thick marine/volcanoclastic sediments. Previous geophysical investigations [5] confirmed that the top of the carbonate basements hidden by younger series has a quite irregular shape and is displaced by a fault system that probably played a significant role in the rise of the magma feeding the volcanic district above mentioned.

A map of the top of the carbonate basement was recently supplied basing on 3D inversion of gravity Bouguer anomalies [8]. CWT2D has been calculated starting from the Bouguer gravity anomaly field in the investigated area. The chosen data set is based on gravity stations collected during several surveys [33,7]. Gravity anomalies were computed by adopting the International formula of the Geodetic Reference System 1980. A reference density of 2.4 g/cm^3 was assumed for the Bouguer and terrain corrections. Computations were made on a residual gravity field achieved after subtraction of a long-wavelength trend to suppress not solvable contributions due to deep causative sources seated beneath and within the lower crust. The selected grid data set is 23×20 km sized, with 0.1 km step grid.

WTMM were calculated in the 3D volume using wavelets of order $q = 2$ and representing, respectively, the modulus maxima of $\nabla(\frac{\partial g_z}{\partial z})$, $\nabla(\frac{\partial g_z}{\partial x})$, $\nabla(\frac{\partial g_z}{\partial y})$ choosing a range of scales [0.0–5.0] km and 0.2 km step. The maxima found by MED2D are shown in Figs. 12a (vertical derivative), 12b (horizontal derivative along x) and 12c (horizontal derivative along y), forming WTMML of clear geological interest. Among the main trends highlighted in the figures, those placed along the southern and the north-eastern sides of the studied area are rather meaningful. They are roughly parallel to the boundaries between Campanian Plain and Apennines (Caserta Mts. and Lattari Mts.) and mark the sharp density contrast between limestones of mesozoic platform and less dense marine/volcanic sediments. These WTMML seem to converge to singularities corresponding to the base of the fault-line scarps, that are due to the downward displacement of the carbonate basement with throws of thousands of meters, and that are hidden by younger series.

A noticeable trend with circular shape is visible in Fig. 12a (vertical derivative) in correspondence of the central axis of the Vesuvius. It is probably related to the presence of a shallow source just beneath the crater already evidenced in previous studies and interpreted as a low density caldera filled not only by pyroclastics but also by shattered lava rocks [8].

A local WTMML analysis has been carried out on the gravity low located near Pompei (South–East of the Somma-Vesuvius). Here, a further subsidence of the carbonate basement locally occurs from a depth of 1000–1500 m down to 2000 m b.s.l. [8]. Two WTMML, localised as shown in Fig. 12c (grey dots), were selected from the y (N–S direction) component of the horizontal derivative for WTMM analysis in the 3D scalogram.

The selected WTMML converge to a singular point located roughly at the centre of the Pompei Trough and at a depth of 2200–2300 m b.s.l. (Fig. 13). Similar results are obtained for other WTMML analysed in the same area. This result is in good agreement with evidences from previous investigations [5,8] resulting only slightly deeper (20%) than suggested from seismic results. This could be explained by supposing a carbonate trough with a round base, because it has proven that a basin with a rather smoothed bottom can yield some over estimation of the depth [11].

The same gravity pattern was analysed by applying the DEXP transformation along two distinct profiles.

The DEXP transformed field was analysed along two profiles (Fig. 11) with Poisson wavelets of various order q, finally selecting $q = 2$. From the analysis of the scale function (Eq. (14)) along the WTMML in the area, a scaling exponent of class C ($\alpha = 0.25$), typical of sources like semi-infinite plane (e.g. thin dike or sill, for geological cases) was found appropriate for most of the sources identified. The DEXP transformed field along the profile I (Fig. 14) shows a large, low density source just in correspondence of the gravity low of Pompei. In the central zone of the Pompei tectonic depression the estimated depth to the bottom of a basin model was 2.5 km (black dot at $x = 5$ km). This result agrees with both the CWT evidences and the model of densities achieved by 3D inversion of gravity data [8]. This is not the only evidence arising from the DEXP because the structural geometry of the carbonate basement is detailed by other features. Two shallow denser sources (singular points) are identified on the opposite sides of the Pompei Trough. Their depth and position correspond, respectively, i) to the southward outcropping carbonate basement at the foot of the Lattari Mts. ($x = 2$ km; $z = 300$ m) and ii) to a small upraised carbonate block ($x = 9.5$ km), already identified northward [8] with depth to the top at about 350 m b.s.l. The section continues northward with another small low density source ($x = 13$ km; $z = 500$ m) whose meaning has to be simply interpreted as local pause of the gradual rise of the carbonate basement. This, finally, outcrops toward the northern end of the profile ($x = 14.5$ km) where another denser source is located just beneath the surface in correspondence of the Caserta Mts. (Apennines).

The analysis along the profile II (Fig. 15) confirms our basin model for the tectonic depression of the mesozoic basement beneath Pompei ($x = 10$ km; $z = 2000$ m). As expected, it identifies other two causative sources (singular points) on the opposite sides of the Pompei Trough: i) a denser source north-westward ($x = 5$ km; $z = 500$ m), where the carbonate

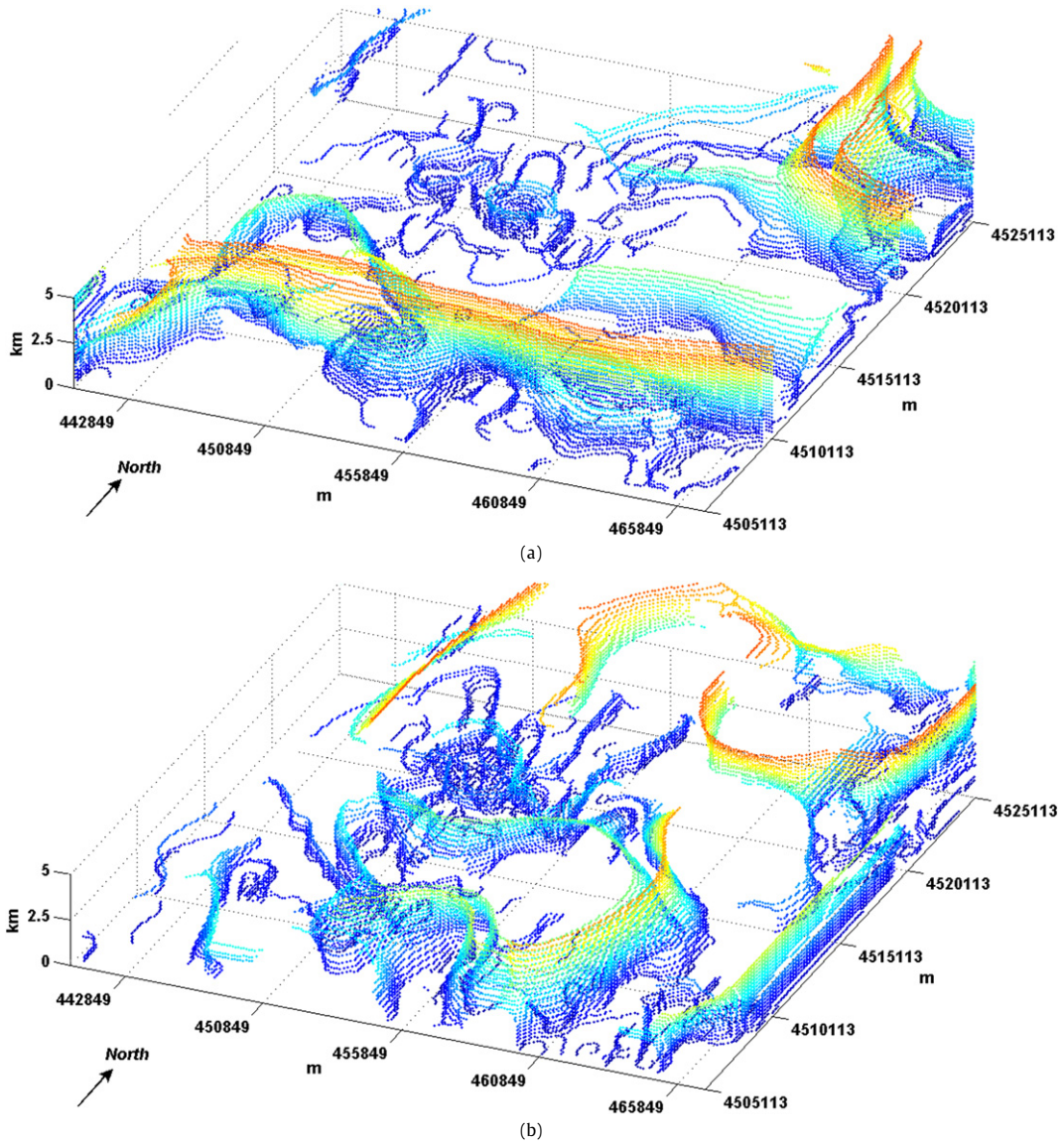

Fig. 12. 3D scalogram of the gravity field in Fig. 11, showing WTMM calculated using wavelets of order $q = 2$ and representing, respectively, the modulus maxima of $\nabla(\frac{\partial g_z}{\partial z})$ (a), $\nabla(\frac{\partial g_z}{\partial x})$ (b), and $\nabla(\frac{\partial g_z}{\partial y})$ (c). Scales range: [0.0–5.0] km; step: 0.2 km. Also shown WTMM (c, grey dots) analysed in Fig. 13 with the geometric method.

basement rises up to a depth to the top of 0.5 km; ii) another high density source shown at the southern end of the profile ($x = 13$ km; $z = 400$ m) where the carbonate basement gets closer to the outcrop near the Lattari Mts.

Briefly, the main features identified by DEXP analysis consists in detecting singularities, which allow the description of a complex pattern of either deep or shallow sources, that is structural highs and lows of the basement due to differential displacement along a normal fault-line system. On the whole, the quantitative reconstruction of the kind and the geometry of the top of the mesozoic carbonate is confirmed by evidences arisen from other geophysical techniques [5,8].

7. Conclusions

In this paper we have analysed the potential fields due to extended geological sources, by the use of the real 2D CWT. Such a 3D space-scale decomposition of potential fields yields different, but coherent, information about their sources (singularities of the potential) when analysing wavelets of different order q are used. Sailhac and Gilbert [29], Saracco et al. [30,31] considering the multipolar expansion of the Newtonian potential, have used 2D wavelets corresponding to the first- and second-order derivatives of 2D Poisson kernel to estimate the barycentre (by the geometrical or best depth method) and the horizontal and vertical extent of the 3D source. In this case it is necessary to hypothesise the geometrical shape (triaxial ellipsoid, cylinder or rectangular prism). In this paper we focused our attention to the WTMM in the 3D scalogram

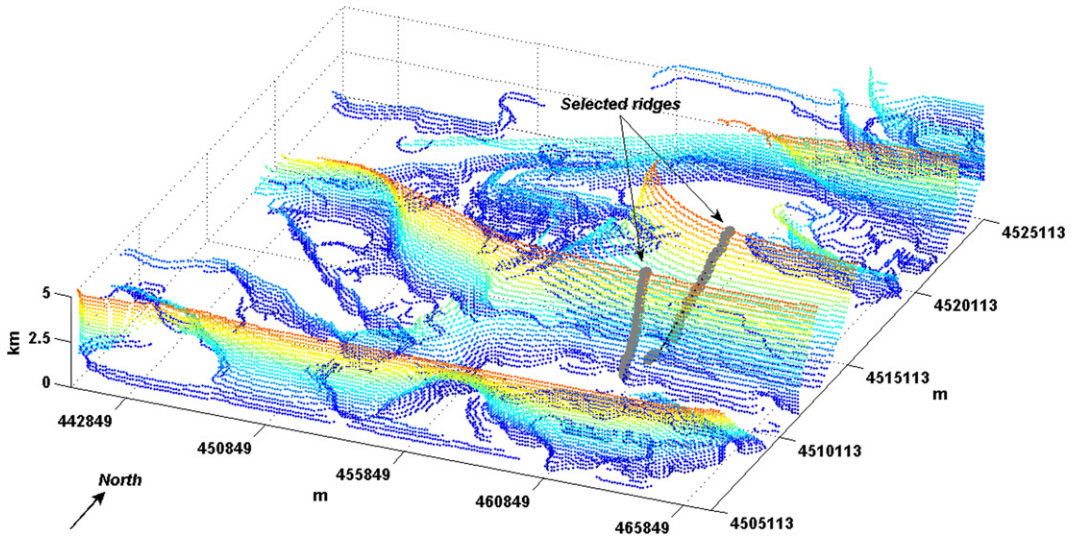

(c)

Fig. 12. *(continued)*

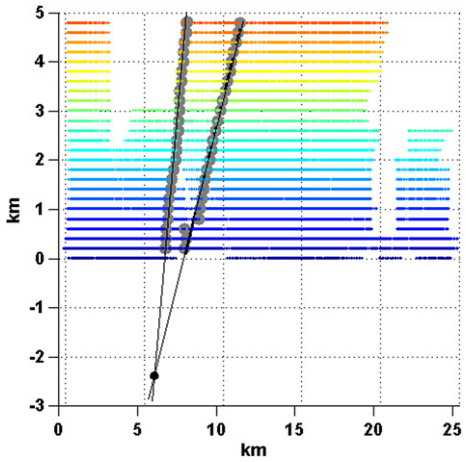

Fig. 13. 3D scalogram section showing the selected WTMML extracted from the 3D scalogram, also shown in Fig. 12c. The best-fit lines converge to a singular point coinciding with the centre of the Pompei Trough, at a 2200–2300 m b.s.l. depth.

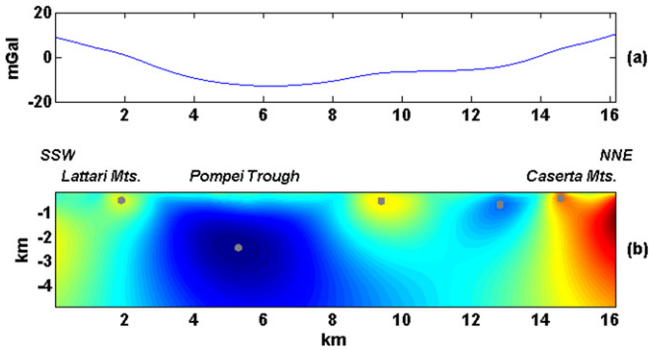

Fig. 14. DEXP transformation applied along the Profile 1, shown in Fig. 11. The gravity field along that profile (a) was DEXP transformed (b) using $q = 2$ and $\alpha = 0.25$. The positions of the identified singularities are marked by black dots.

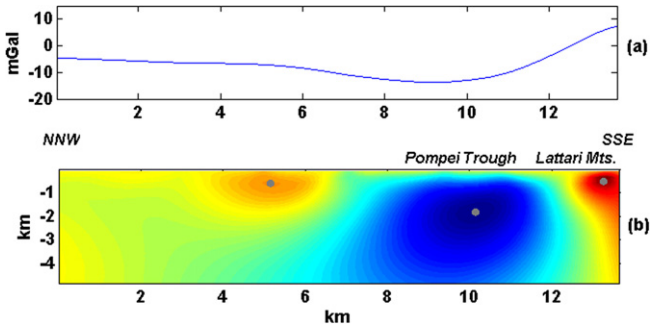

Fig. 15. DEXP transformation applied along the Profile 2, shown in Fig. 11. The gravity field along that profile (a) was DEXP transformed (b) using $q = 2$ and $\alpha = 0.25$. The positions of the identified singularities are marked by black dots.

produced by using 2D Poissonian wavelets of different order, to the end of estimate the depth of source-related edges, in x–y plane, and the depth, of specific parts of 3D extended bodies. This paper shows that CWT is able not only to describe the main average features of an extended source, according to previous results, but also to get a more detailed description of its local portions, if they may be associated to singularities of high order derivatives of the field. We showed that, by using the geometrical method with an appropriate order for the analysing wavelets, it is possible to obtain information also about the bottom of the geological body, whenever the interference is not too strong. Generally the best estimations are obtained at the minimum order of derivation useful to visualise WTMML, even though the interference occurring near the vertices of the body can prevent the location of some edges and reduce the number of suitable scales for estimating the depth. In such cases, wavelets of higher orders can provide better results, whenever the signal-to-noise ratio is not too strong. The CWT2D method was also applied to real data: the gravity anomaly map of the Vesuvius area (Southern Italy), where it yielded impressive WTMM and a meaningful estimation of the depth of the carbonate basement buried beneath the series of younger volcanoclastic/marine sediments. The results are in good agreement with evidences from previous seismic and gravity investigations. We also integrated our CWT results by using the DEXP transformation. When both CWT and DEXP transformation are expressed in terms of q-order derivatives of the fields at various scales (Eqs. (14) and (15)), they show a similar mathematical form, the main difference being their scale power law factors. The CWT power law factor depends only on the derivation order, while the DEXP transformation factor depends also on the so-called structural index N, a source-dependent parameter which is the negative of the homogeneity degree of the field. DEXP transformation was applied to a couple of profiles in the Campanian Plain giving consistent results about the behaviour of the underlying carbonate basement.

Appendix A. Multiscale Edge Detection 2D

One of the most efficient algorithms in the search of the edges of an image is that of Canny [6].

Let $f(x, y)$ an image, the gradient of f is defined by:

$$\nabla f = \left(\frac{\partial f}{\partial x}, \frac{\partial f}{\partial y} \right) \tag{A.1}$$

whose Mf modulus and Af argument are:

$$Mf = \sqrt{\left(\frac{\partial f}{\partial x} \right)^2 + \left(\frac{\partial f}{\partial y} \right)^2} \tag{A.2}$$

$$Af = \mathrm{tg}^{-1} \left(\frac{\partial f / \partial y}{\partial f / \partial x} \right) \tag{A.3}$$

The Canny algorithm defines the edges of an image f as the points where Mf is locally maximum in the Af direction.

Mallat and Zhong [17], Mallat and Hwang [16] have rephrased the technique of Canny [6] in terms of the CWT2D, considering as wavelets the partial derivatives along x and y direction of a smoothing function $\phi(x, y)$ (Arneodo [1]):

$$\psi^x(x, y) = \frac{\partial \phi(x, y)}{\partial x} \quad \text{and} \quad \psi^y(x, y) = \frac{\partial \phi(x, y)}{\partial y} \tag{A.4}$$

and

$$\psi_a^x = \frac{\psi^x(x/a, y/a)}{a^2} = a \frac{\partial}{\partial x} \frac{\phi(x/a, y/a)}{a^2}; \qquad \psi_a^y = \frac{\psi^y(x/a, y/a)}{a^2} = a \frac{\partial}{\partial y} \frac{\phi(x/a, y/a)}{a^2} \tag{A.5}$$

For a function $f(x, y) \in L^2(R^2)$, the CWT2D has two components and therefore it can be expressed in vectorial form:

$$\mathbf{W}f(a,\mathbf{x}) = \begin{pmatrix} W_x f = \psi_a^x(\mathbf{x}) * f(\mathbf{x}) \\ W_y f = \psi_a^y(\mathbf{x}) * f(\mathbf{x}) \end{pmatrix} \tag{A.6}$$

Taking into account Eq. (A.5), we may rewrite Eq. (A.6) in the compact form:

$$\mathbf{W}f(a,\mathbf{x}) = a\nabla\{\phi_a * f\} \tag{A.7}$$

Eq. (A.7) defines the CWT2D as the gradient of a smoothed version of the function $f(\mathbf{x})$, obtained by its convolution with ϕ_a, that is with ϕ dilated and scaled at the scale a.

The Canny's algorithm expressed in terms of the CWT2D yields the followings relationships:

$$\mathbf{W}f(a,\mathbf{x}) = \big(Mf(a,\mathbf{x}), Af(a,\mathbf{x})\big) \tag{A.8}$$

where

$$Mf(a,\mathbf{x}) = \big|\mathbf{W}f(a,\mathbf{x})\big| = \big[\big(W_x f(a,\mathbf{x})\big)^2 + \big(W_y f(a,\mathbf{x})\big)^2\big]^{1/2} \tag{A.9}$$

and

$$Af(a,\mathbf{x}) = \mathrm{tg}^{-1}\big[\big(W_y f(a,\mathbf{x})\big)\big/\big(W_x f(a,\mathbf{x})\big)\big] \tag{A.10}$$

Appendix B. Canny's algorithm for order $q > 1$

If $q = 1$, defining as wavelets

$$\psi_x = \frac{\partial p}{\partial x}; \qquad \psi_y = \frac{\partial p}{\partial y} \tag{B.1}$$

we obtain:

$$\mathbf{W}f(a,\mathbf{x}) = a\nabla g_z(\mathbf{x}) = a\left(\frac{\partial g_z}{\partial x}, \frac{\partial g_z}{\partial y}\right) \tag{B.2}$$

$$Mf(a,\mathbf{x}) = a\sqrt{\left(\frac{\partial g_z}{\partial x}\right)^2 + \left(\frac{\partial g_z}{\partial y}\right)^2} = \sqrt{W_x^2 + W_y^2} \tag{B.3}$$

$$Af = \mathrm{tg}^{-1}\frac{W_y}{W_x} \tag{B.4}$$

and the WTMM correspond to the modulus maxima of the gradient of g_z at different levels.

If $q = 2$, it is possible to define the analysing wavelet in different way. Selecting as wavelet:

$$\psi_{xx} = \frac{\partial^2 p}{\partial x^2}; \qquad \psi_{yy} = \frac{\partial^2 p}{\partial y^2} \tag{B.5}$$

we obtain:

$$\mathbf{W}f(a,\mathbf{x}) = a^2\nabla^{(2)} g_z(\mathbf{x}) = a^2\left(\frac{\partial^2 g_z}{\partial x^2}, \frac{\partial^2 g_z}{\partial y^2}\right) \tag{B.6}$$

$$Mf(a,\mathbf{x}) = a^2\sqrt{\left(\frac{\partial^2 g_z}{\partial x^2}\right)^2 + \left(\frac{\partial^2 g_z}{\partial y^2}\right)^2} = \sqrt{W_{xx}^2 + W_{yy}^2} \tag{B.7}$$

$$Af = \mathrm{tg}^{-1}\frac{W_{yy}}{W_{xx}} \tag{B.8}$$

and the WTMM correspond to the modulus maxima of the second gradient of g_z. Selecting as wavelet:

$$\psi_{xx} = \frac{\partial^2 p}{\partial x^2}; \qquad \psi_{yx} = \frac{\partial^2 p}{\partial y \partial x} \tag{B.9}$$

we obtain:

$$\mathbf{W}f(a,\mathbf{x}) = a^2\nabla\left(\frac{\partial g_z}{\partial x}\right) = a^2\left(\frac{\partial^2 g_z}{\partial x^2}, \frac{\partial^2 g_z}{\partial y \partial x}\right) \tag{B.10}$$

$$Mf(a,\mathbf{x}) = a^2\sqrt{\left(\frac{\partial^2 g_z}{\partial x^2}\right)^2 + \left(\frac{\partial^2 g_z}{\partial y \partial x}\right)^2} = \sqrt{W_{xx}^2 + W_{yx}^2} \tag{B.11}$$

$$Af = \mathrm{tg}^{-1}\frac{W_{yx}}{W_{xx}} \tag{B.12}$$

and the WTMM correspond to the modulus maxima of the gradient of $\frac{\partial g_z}{\partial x}$.

In the same way using as wavelet:

$$\psi_{yy} = \frac{\partial^2 p}{\partial y^2}; \qquad \psi_{xy} = \frac{\partial^2 p}{\partial x \partial y} \tag{B.13}$$

the WTMM correspond to the modulus maxima of the gradient of $\frac{\partial g_z}{\partial y}$.

Similar relationships can be found for wavelet of order $q > 2$. Using wavelets of order derivative q the CWT2D will depend to the q-partial derivative of g_z.

References

[1] A. Arneodo, N. Decoster, S.G. Roux, A wavelet-based method for multifractals image analysis. I. Methodology and test applications on isotropic and anisotropic random rough surfaces, Eur. Phys. J. B 15 (2000) 567–600.
[2] R.J. Blakely, R.W. Simpson, Locating edges of source bodies from magnetic or gravity anomalies, Geophysics 51 (1986) 1494–1498.
[3] J.P. Antoine, R. Murenzi, P. Vandergheynst, S.T. Ali, Two-Dimensional Wavelets and Their Relatives, Cambridge University Press, Cambridge, UK, 2004.
[4] R.J. Blakely, Potential Theory in Gravity and Magnetic Applications, Cambridge University Press, 1995.
[5] P.P.G. Bruno, A. Rapolla, Study of the sub-surface structure of Somma-Vesuvius Italy by seismic reflection data, J. Volcanol. Geotherm. Res. 92 (1999) 373–387.
[6] J. Canny, A computational approach to edge detection, IEEE Trans. Pattern Anal. Mach. Intell. PAMI-8 (1986) 679–698.
[7] E. Cassano, P. La Torre, Geophysics, in: R. Santacroce (Ed.), Somma-Vesuvius, in: C.N.R. Quad. Ric. Sci., vol. 114 (8), 1987, pp. 175–192.
[8] F. Cella, M. Fedi, G. Florio, M. Grimaldi, A. Rapolla, Shallow structure of the Somma-Vesuvius volcano from 3D inversion of gravity data, J. Volcanol. Geotherm. Res. 161 (2007) 303–317.
[9] B. De Vivo, R. Scandone, R. Trigila, Mount Vesuvius, J. Volcanol. Geotherm. Res. 58 (1993) 1–381.
[10] M. Fedi, A. Rapolla, 3-D inversion of gravity and magnetic data with depth resolution, Geophysics 64 (1999) 452–460.
[11] M. Fedi, R. Primiceri, T. Quarta, A.V. Villani, Joint application of continuous and discrete wavelet transform on gravity data to identify shallow and deep sources, Geophys. J. Int. 156 (2004) 7–21.
[12] M. Fedi, Multiscale derivative analysis: A new tool to enhance detection of gravity source boundaries at various scales, Geophys. Res. Lett. 29 (2) (2002) 16-1–16-4.
[13] M. Fedi, DEXP: A fast method to determine the depth and the structural index of potential fields sources, Geophysics 72 (1) (2007) I1–I11, doi:10.1190/1.2399452.
[14] M. Fedi, G. Florio, T.A.M. Quarta, Multiridge analysis of potential fields: Geometric method and reduced Euler deconvolution, Geophysics 74 (4) (2009) L53–L65.
[15] P. Hornby, F. Boschetti, F.G. Horowitz, Analysis of Potential field data in the wavelet domain, Geophys. J. Int. 137 (1999) 175–196.
[16] S. Mallat, W.L. Hwang, Singularity detection and processing with wavelets, IEEE Trans. Inform. Theory 38 (2) (1992) 617–643.
[17] S. Mallat, S. Zhong, Characterization of signals from multiscale edges, IEEE Trans. Pattern Anal. Mach. Intell. 14 (7) (1992) 710–732.
[18] S. Mallat, A Wavelet Tour of Signal Processing, Academic Press, 1998.
[19] S. Maus, V.P. Dimri, Scaling properties of potential fields due to scaling sources, Geophys. Res. Lett. 21 (1994) 891–894.
[20] F. Moreau, D. Gibert, M. Holschneider, G. Saracco, Wavelet analysis of potential fields, Inverse Problems 13 (1997) 165–178.
[21] F. Moreau, D. Gibert, M. Holschneider, G. Saracco, Identification of sources of potential fields with the continuous wavelet transform: basic theory, J. Geophys. Res. 104 (B3) (1999) 5003–5013.
[22] F. Mostardini, S. Merlini, Appennino centro-meridionale. Sezioni geologiche e proposta di modello strutturale, Mem. Soc. Geol. Ital. 35 (1986) 177–202.
[23] M.K. Paul, D. Sukumar, B. Buddhadeb, Direct interpretation of two-dimensional structural faults from gravity data, Geophysics XXXI (5) (1966) 940–948.
[24] M. Pilkington, J.P. Todoeschuck, Fractal magnetization of continental crust, Geophys. Res. Lett. 20 (1993) 627–630.
[25] A.B. Reid, J.M. Allsop, H. Granser, A.J. Millett, I.W. Somerton, Magnetic interpretation in three dimensions using Euler deconvolution, Geophysics 55 (1990) 80–91.
[26] G. Rolandi, P. Petrosino, J. McGeehin, The interplinian activity at Somma-Vesuvius in the last 3500 years, J. Volcanol. Geotherm. Res. 82 (1998) 19–52.
[27] D. Ravat, Analysis of the Euler method and its applicability in environmental magnetic investigations, J. Environ. Eng. Geophys. 1 (1996) 229–238.
[28] P. Sailhac, A. Galdeano, D. Gibert, F. Moreau, C. Delor, Identification of sources of potential fields with the continuous wavelet transform: Complex wavelet and application aeromagnetic profiles in French Guiana, J. Geophys. Res. 155 (B8) (2000) 19455–19475.
[29] P. Sailhac, D. Gilbert, Identification of sources of potential fields with the continuous wavelet transform: Two dimensional wavelets and multipolar approximations, J. Geophys. Res. 108 (2003) 2296–2306.
[30] G. Saracco, P. Labazuy, F. Moreau, Localization of self-potential sources in volcano-electric effect with complex continuous wavelet transform and electrical tomography methods for an active volcano, Geophys. Res. Lett. 31 (2004) L12610, doi:10.1029/2004GL019554.
[31] G. Saracco, F. Moreau, P.E. Mathe, D. Hermitte, J.M. Michel, Multi-scale tomography of buried magnetic structures. Its use in the localization and characterization of archaeological structures, Geophys. J. Int. 171 (1) (2007) 87–103.
[32] M. Talwani, L. Worzel, M. Landisman, Rapid gravity computation for two-dimensional bodies with application to Mendocino submarine fracture zone, J. Geophys. Res. 64 (1959) 49–59.
[33] G. Tribalto, A. Maino, Rilevamento gravimetrico della zona circumvesuviana, Ann. Oss. Vesuv. IV (sesta serie) (1962) 134–172.
[34] C. Zhang, M.F. Mushayandebvu, A.B. Reid, J.D. Fairhead, E. Odegard, Euler deconvolution of gravity tensor gradient data, Geophysics 65 (2000) 512–520.